



UNIVERSITY OF CAPE TOWN

PHY3004W

3RD YEAR PHYSICS GROUP PROJECT

Characterisation of the HR++ Scanner at iThemba Labs for PEPT

Authors:

Joshua Browne, Kira Hanmer, Batsirayi Ziki, Zahra Mohamed,
Tswelopele Moshe, Khalid Amardien, Mikayla Chaplin, Mothibi
Mathivha, Tasmiyah Rawoot, Zayd Pandit, Talente Mzindle, Austin
Conolly, Salmaan Barday

Supervised by:

Dr Tom Leadbeater
Mike van Heerden

November 2021

1 Abstract

Positron Emission Particle Tracking (PEPT) is a technique used to track the motion and position of objects using radioactive sources. The equipment used to track a particle plays a large role in this and the quality of said equipment can affect the precision and accuracy of the tracking. This paper will thus be characterising a particular camera system, the HR++ located at iThemba labs, and investigating characteristics such as the accuracy, precision and sensitivity. This will help determine what can and cannot be done with this camera system and where improvements can be made to it.

Contents

1 Abstract	1
2 Introduction and Theory	3
3 Optimal Fractional Values	7
3.1 Theory	7
3.2 Method	7
3.3 Analysis	8
4 Randoms	9
4.1 Theory	9
4.2 Method	10
4.3 Results and Analysis	10
5 Scatter Fraction	11
6 Sensitivity and Efficiency	14
6.1 Theory	14
6.2 Results and Analysis	15
6.2.1 Sensitivity	15
6.2.2 Efficiency	17
7 Spatial Resolution	18
7.1 Theory	18
7.2 Results and Analysis	20
8 Image Quality	23
8.1 Theory	23
8.2 Method and Analysis	24
9 Accuracy and Precision	27

9.1	Theory	27
9.2	Method	27
9.3	Analysis	28
10	Deadtime	33
10.1	Theory	33
10.2	Method	33
10.3	Analysis	34
11	Conclusions	36
	References	38
	Appendix	40

2 Introduction and Theory

Positron Emission Particle Tracking (PEPT) is a nuclear technique that can be used to measure the trajectory of a particle from a source that undergoes radioactive decay in which a positron is produced. The positron produced will annihilate with an electron, resulting in the production of a pair of gamma rays of the same energy (511 keV each). If the 511 keV gamma rays are detected in coincidence by a modified positron emission tomography (PET) camera, then their linear trajectory defines a line of response (LOR). We deduce that the origin of the gamma rays must have then occurred somewhere along this straight line. In almost all cases, multiple LORs are produced as a result of multiple decays occurring within a tracer, and a least squares minimisation convergence approach is then used to determine the possible centroid of the tracer particle, analogous to triangulation.

Ideally, only two LORs are needed, if the source is point-like. However, most sources are not point-like and there are measurements of false LORs which come from the detection of gamma rays not associated with an annihilation event, such as gamma rays that have undergone Compton scattering [2] or Random coincidences (to be discussed in section 4). This means that a large number of LORs are required to triangulate the position of the moving source. We use an iterative algorithm to find the position of the source. The algorithm used to triangulate the position works by calculating the minimum distance point m in a set S of LORs for which the sum $\sum_s \delta_i(m)$ is at a minimum, where $\delta_i(m)$ is the nearest distance of the i^{th} LOR from m . A small fraction of the LORs that lie farthest from m are then removed from the set as these are most likely corrupt events. From the remaining set of LORs, a new m is created and the same process is then repeated for the new set of LORs. This process is repeated until the remaining number of LORs in the set is reduced to a fraction of the initial number of events fN where f is a specified value between 0 and 1. Figure 1 demonstrates how the algorithm works.

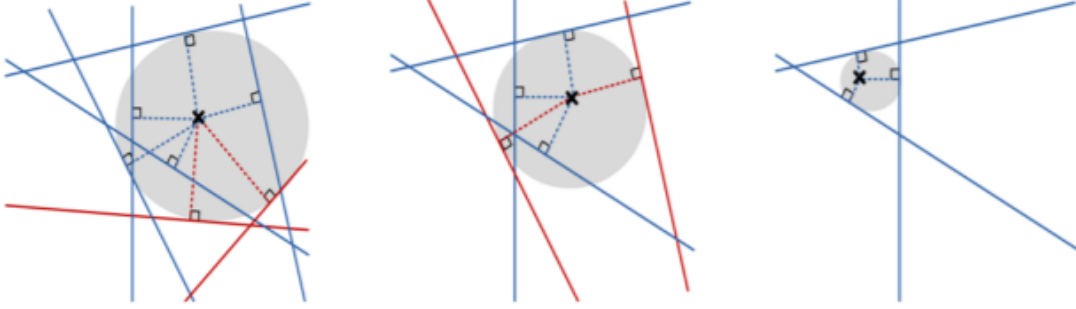


Figure 1: The depiction of the iterative triangulation algorithm that removes the corrupted LORs after each iteration[6].

The PEPT Cape Town facility at iThemba LABS became the second operational PEPT facility and a range of PEPT applications have been explored over the last few years at this facility, such as powder mixing and fluid behaviour in granular beds [2]. The facility houses the ECAT HR++ (Model: CTI/Siemens 966) PET camera [2].

The HR++ has been designed to achieve high resolution and high sensitivity for PET research. The HR++'s ring geometry is larger than other standard ring geometry PET cameras; it has 48 rings made of bismuth germinate detector elements with a ring diameter of 82 cm, a radial field of view of radius 30 cm and an axial field of view of 23.4 cm. Each of these detector elements has dimensions 4.39 mm transaxial, 4.05 mm axial and 30 mm deep, and the elements are grouped in 8x8 blocks. Each detector block is connected to a detector bucket or interchangeably module which contains the analogue electronic front end to interface to the photomultiplier tubes, position and time digitisation [12]. There are currently 34 modules, with modules 2 and 28 missing from the system.

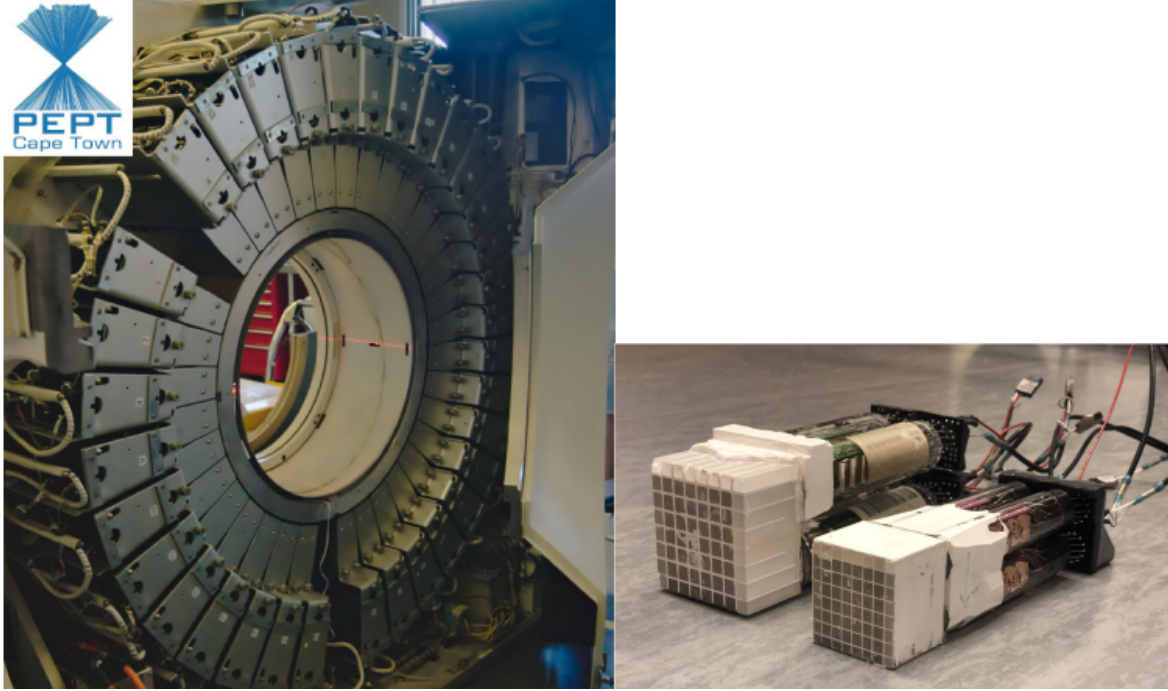


Figure 2: Left: The UCT HR++ positron camera consisting of 36 modules with 12 detector blocks for each module, with each detector block consisting of 8×8 crystal elements. Two modules have been removed from the system in this image. Right: Inside cutaway of the 8×8 detector block concept, with the larger (back) unit belonging to the older detector type; the HR++ uses the newer, high resolution, version shown in the front. The newer unit has crystals with the following dimensions: 4.39 mm transaxial \times 4.05 mm axial \times 30 mm deep [12].

The uncertainty in PEPT measurements with the HR++ depends significantly on the geometry and attenuation of the system being studied, the size and activity of the source, and the speed with which the tracer is moving [10]. We aim to evaluate the performance of the HR++ scanner for PEPT. This HR++ scanner has recently been serviced and calibrated, with the aim of improving its performance. This paper covers multiple parameters such as spatial resolution, optimal fractional values, deadtime, count losses, accuracy, corrections, sensitivity, efficiency, and image quality in order to characterise the HR++. Spatial resolution refers to the precision with which the PEPT camera can measure the instantaneous position of the tracer particle, while optimal fractional values focus on obtaining the optimal percentage of remaining coincidences when calculating position. The accuracy of the scanner refers to how well it measures the position of the tracer particle, and any discrepancies are then identified and corrected. When a photon Compton scatters from an electron, scattering occurs. The scatter fraction is defined as the ratio of scattered events to true events. Random events occur when the detector registers uncorrelated events as coincidence events.

Additionally, the efficiency and sensitivity are analysed, and they explain how efficient the system is at detecting gamma rays. Finally, a deadtime parameter is determined, which refers to the amount of time after an event is detected, during which no new events can be detected.

Motivation

PEPT is a useful technique and exploring the performance parameters of one of the major PEPT scanners in the world is key to further scientific progress in this field. The PEPT scanner at iThemba labs in Cape Town has made a significant contribution to research in particle flow in aggressive environments [1]. The improved upon HR++ ring has the potential for more refined research. By measuring the performance parameters of this detector system (the second of its kind next to the facility in Birmingham), we will aid the measurements and analysis of all future research done using this detector system. A group of final-year undergraduate physics students is the ideal choice to conduct this experiment as the group is large enough to explore many significant aspects of the HR++ simultaneously. This opportunity also allows the students to gain research experience in exchange for useful information that will be vital knowledge in further, more specialized projects. The fact that this facility is one local to and operated by the University of Cape Town means that this investigation provides an opportunity for students to do some real scientific research using a highly advanced facility in their own city (an opportunity that is slim in any other centre such as iThemba labs in the world). Due to COVID restrictions, experiments will not be conducted by the students themselves, and instead will be conducted by a member of PEPT at iThemba Labs with great experience.

Previous research

Previous research has been done on evaluating the performance of PEPT scanners, which includes the HR++ scanner at iThemba labs [2],[1]. This research has fortunately been published, and was at our disposal to reference and guide us in the analysis and report write-up. In addition to this, we found published papers of PET (positron emission tomography) detectors, which are also relevant to the investigation, since PEPT scanners use advanced PET cameras. PEPT is a variant of PET in that PET focuses on a single tracer particle which is used to produce an image, while PEPT aims to accurately determine the location of the particle as it moves through the equipment [15]. The topics which many of these papers focus on include sensitivity, scatter fraction, spatial resolution, count rate, random events, image quality, correction, accuracy and deadtime [7], [5]. Together, these parameters will provide a thorough performance evaluation of the HR++ scanner. All of these parameters are those which we wish to

investigate. However, as the aim is different to that of PEPT, the methods with which we measure the performance parameters will be altered from those used in PET.

3 Optimal Fractional Values

3.1 Theory

The aim is to remove corrupt events from the original set of all events, and thereby find the location of the particle. This can be done using the location algorithm *ctrack.exe* [12]. These corrupt events' trajectories are generally found further away from the rest of the trajectories. Thus, by removing the furthest trajectories and using an iterative process we can discard trajectories until we believe that most of the corrupt events have been removed, as shown in figure 1. This allows for a more precise and accurate measure of the location of the particle.

3.2 Method

A ^{22}Na source with an activity of 12 μCi , was placed at the center of the scanner and the data was recorded into a file.

The uncertainty associated with an individual location can be calculated for each spatial coordinate. This is done by taking the standard deviation of the set of locations calculated by *ctrack* and the equation of which is given by

$$u(x) = \sqrt{\frac{\sum (x_i - \bar{x})^2}{n}}; \quad u(y) = \sqrt{\frac{\sum (y_i - \bar{y})^2}{n}}; \quad u(z) = \sqrt{\frac{\sum (z_i - \bar{z})^2}{n}} \quad (1)$$

where n is the number of measured locations and \bar{x} , \bar{y} and \bar{z} are the mean values. *ctrack* was given instructions on what N value to use as well as to run different values of f in order to find f_{opt} , which is the value of f which minimizes the uncertainty. It then stored the locations obtained in a text file, which was read by python and used to calculate the 3D standard deviation σ_{3D} by propagating the standard deviations of the x , y and z coordinates, i.e. using the equation

$$\sigma_{3D} = \sqrt{u(x)^2 + u(y)^2 + u(z)^2} \quad (2)$$

This was run for f from 10 to 90 in steps of 2 and for $N = 100, 250$, and 500 as seen in Figure 3. When obtaining Figure 4, *ctrack* was used once more with the same data as before with the difference being that f_{opt} was kept constant at $f_{opt} = 50$ and N was varied from 10 to 500 in steps of 5 and the σ_{3D} was stored for each N value.

3.3 Analysis

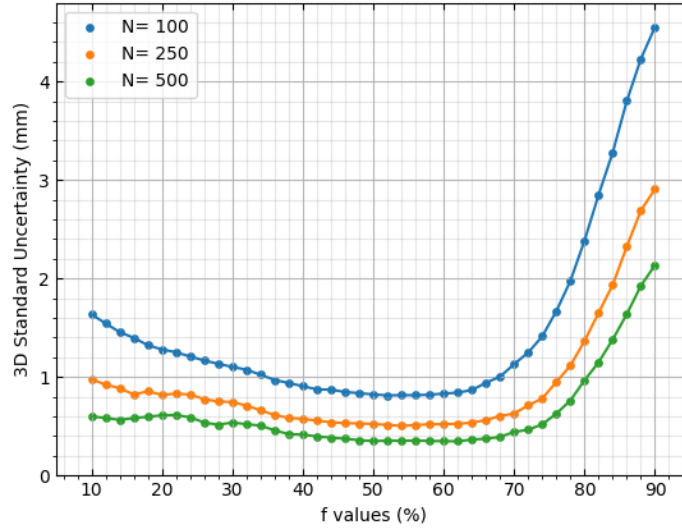


Figure 3: The graph above shows the 3D standard deviation σ_{3D} vs the fractional values f for $N=100$, $N=250$ and $N=300$

When looking at figure 3, the general trend of the fractional values f plotted is as expected. There is a decrease in σ_{3D} as we increase f , until some optimal fraction value f_{opt} is reached, at which point the σ_{3D} has been minimised. After this point, any further increase of f will result in an increase of σ_{3D} .

Through observation we see that the graph plateaus between $f = 50$ and $f = 65$. Between these values the uncertainty of the location of the particle is minimized greatly. The optimal fractional value was chosen to be $f_{opt} = 50$ due to it minimizing the uncertainty the most.

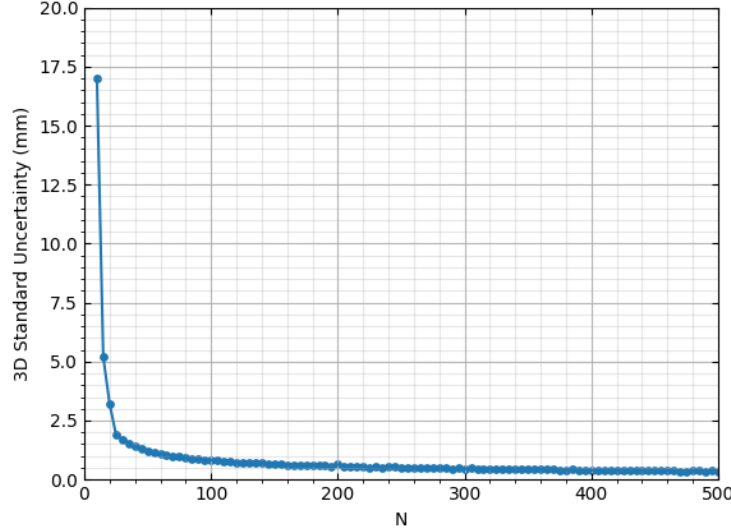


Figure 4: This graph shows the inversely proportional relationship between N and the 3D standard deviation for $f_{opt} = 50$

Precision Δ is given by [19]:

$$\Delta = \frac{w}{\sqrt{fN}} \quad (3)$$

where w is the spacial resolution of the detection system, which is measured to be close to 5mm [20].

Looking at $f_{opt} = 50$ in Figure 4, we observe the expected inverse relation between precision and N (expected theoretically when looking at the equation 3).

For a stationary particle, having a larger N value will improve results of precision and accuracy of the location. However, the disadvantages of using a larger N value include less accurate and precise tracking of moving particles, as their locations will be measured less often.

4 Randoms

4.1 Theory

In a PEPT detector system, any two gamma detections are regarded to be in coincidence if they are detected within a resolving time of 2τ . For the HR++, $\tau = 12$ ns. It is not possible to simultaneously detect photons emitted from the same positron-electron annihilation event. This is due to many factors, such as the drift and overall response-time of the BGO scintillator in each detector. Random events occur when

two (or more) annihilations occur temporally close enough causing the detector to register uncorrelated events as coincidence events due to the fact that photons from these uncorrelated events are detected within the resolving time of the detector system [22].

Moreover, time-resolution is further limited by other physical features of the detector system, like how long the detector takes to form a pulse (100s of ps), how long said pulse takes to be electronically processed (ns) and digitising the signal to be processed and stored(ns).

4.2 Method

Data with both random and coincidence events are called prompt data. Prompt data are collected by opening the coincidence gate 6 ns before an event, with an event occurring at the 0 ns mark. The gate remains open for another 6 ns and, should another event be detected in this window, it is then regarded as part of the prompt data. This includes randoms. The randoms are statistically isolated by delaying the gate. In the case of the HR++ this isolation is achieved by delaying the gate with a window of 64 μ s to obtain the delayed rates events.

4.3 Results and Analysis

We expect the count rate to follow a model given by:

$$R = (2 \times \tau) R_s^2 \quad (4)$$

where $R_s = S/(1 - S \times D_t)$. Here, D_t is the deadtime, and S is the rate of singles. τ for this detector system is 12ns which is the time coincidence window. We see a reasonable trend in the data appropriate to this model, however, the experiment could not be carried out over a wide range of activity to discern the point of inflection, never mind the turning point. Therefore, the deadtime could not be estimated and the model could not be fully realised. We can conclude, however, from this data, that sources of less than or equal to 1 200 μ Ci are reasonable to image or collect PEPT related data from and the point at which the randoms may overwhelm the prompts is not reached within the scope of this experiment.

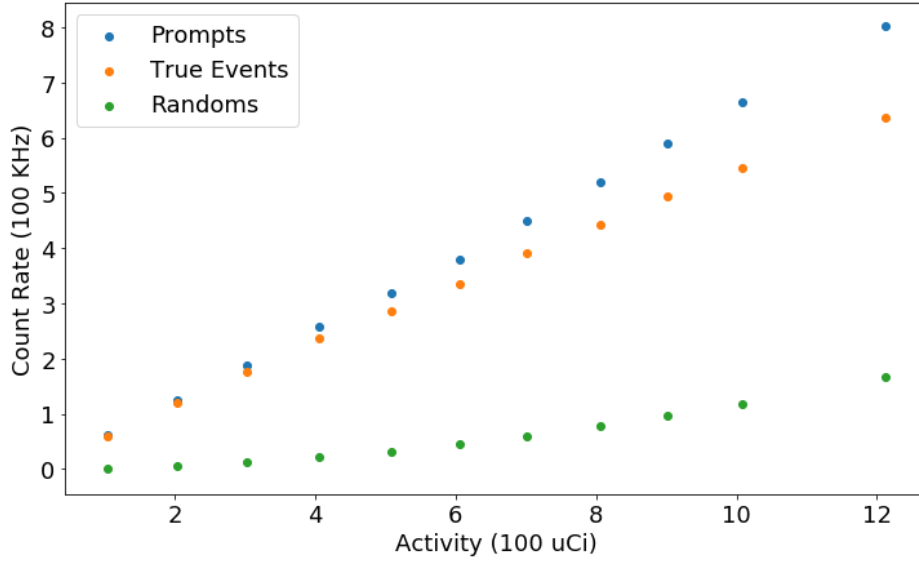


Figure 5: Coincidence rates for the prompts, the true events and random events as a function of activity. The randoms are isolated by using a delayed coincidence window technique [17]. Here, the gate is delayed for 64 microseconds and the resulting count rate is subtracted from the prompts to attain the true events.

5 Scatter Fraction

Theory

Scattering occurs when a photon Compton Scatters from an electron in a medium. Due to the coincidence window, the detector may attribute a scattered photon, rightly so, with its pair but may form an invalid Line of Response since it assumes there was no scattering. The scattering fraction is defined as the ratio of scattered events to the true events. The scatter fraction depends on :

- scattering within the object containing the radionuclide [16],
- activity of the source,
- scattering within the detectors [16],
- the amount of scattering material present in the system [18].

In PEPT experiments, the source can be surrounded by a considerable amount of material, which scatters the emerging photons [18]. Random and scatter events can be discarded by iteration and they do not contribute towards calculating the source location. The precision in location changes as a function of the amount of scattering taking place, and is expected to degrade as scattering increases. f_{opt} is then calculated

as we vary the amount of scattering and a change in the uncertainty value will be observed as the scattering increases. Once the effects of scattering have been analysed, it is possible to account for scattering in this specific detector.

Method

Firstly, measurements of a stationary source were taken at various locations. Measurements were taken of a bare source and then repeat measurements were taken with a source surrounded by scattering material. The scattering material used was water, and we surrounded the source by placing it in a container filled with water. The diameter of the container was 20 cm. For the bare source we used a ^{22}Na source which had an activity of 12 μCi and for the source placed in water, we used ^{68}Ga , which had an activity of 534 μCi .

Table 1 (in the Appendix) shows the coordinates of each location number of the detector and figure 6 shows the locations relative to the HR++.

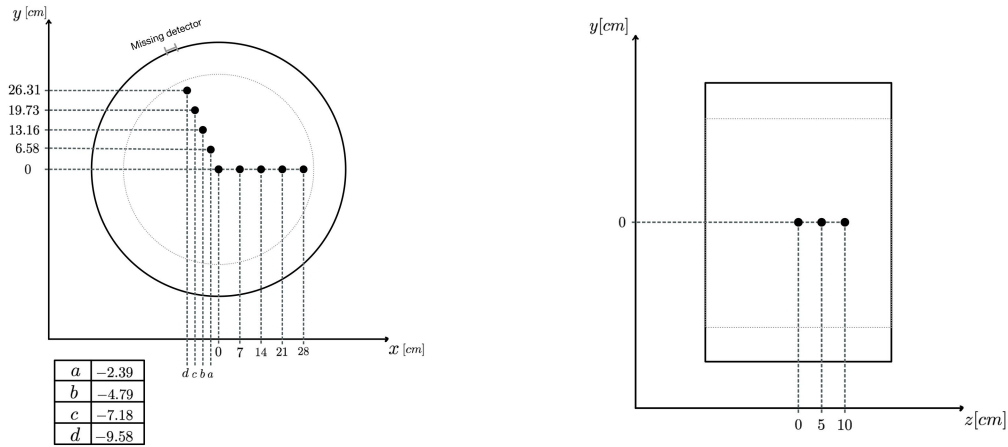


Figure 6: Diagram showing (a) the radial and (b) the axial positions at which the source was placed for each measurement.

Analysis

To calculate the relative uncertainty of the i^{th} measured location (x_i, y_i, z_i) we use equation 1.

Since ^{22}Na has a different activity from ^{68}Ga , the n values are different. Thus, in order to compare them we ensured that the n values for both sources were the same by using *ctrack* and setting the total number of events observed to be the same. It was possible to compare them since ^{22}Na and ^{68}Ga have similar nuclear properties. Figures 7a-7c present locations (x, y, z) measured for the stationary sources. Figure 7d shows the average error measurement for each source at the various locations in the detector.

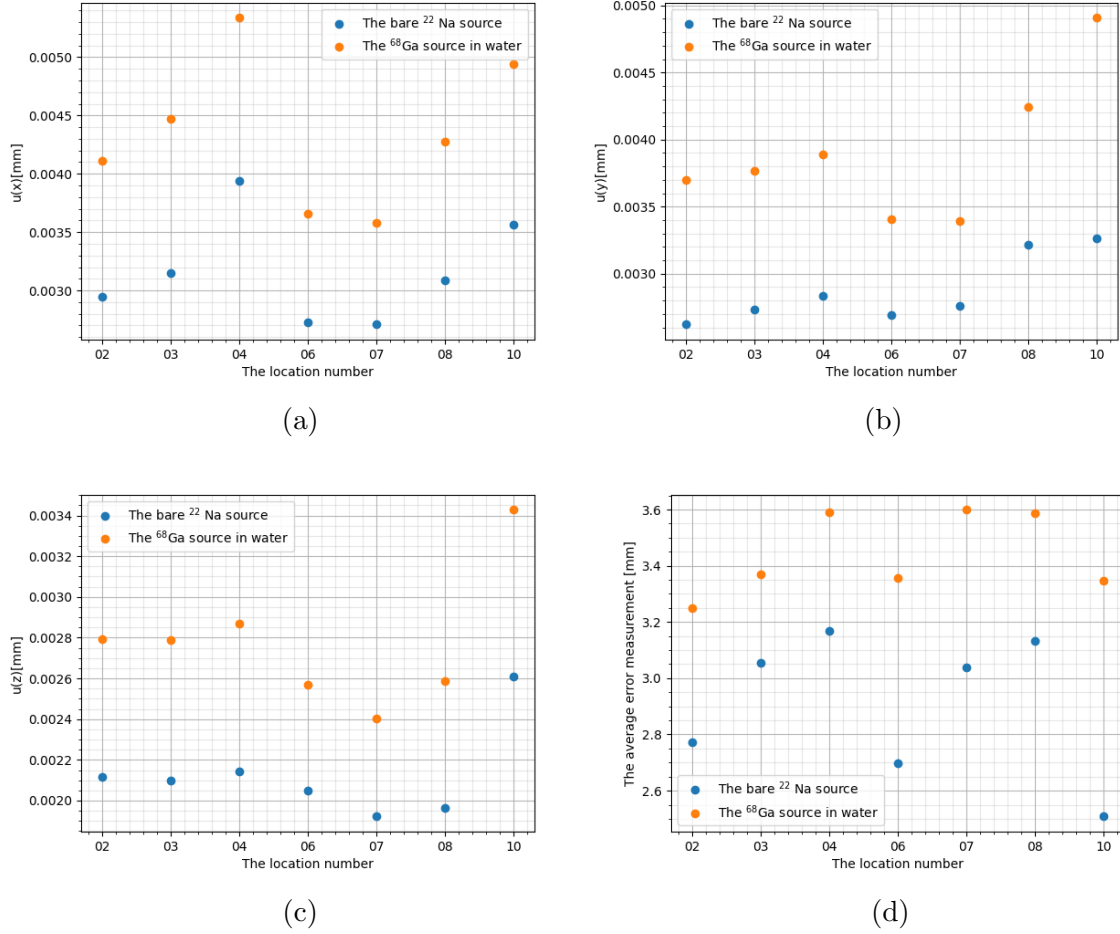


Figure 7: Relative statistical uncertainties u in the coordinates (a) x ; (b) y ; and (c) z , measured for the stationary sources at various locations in the detector. (d) shows the average error measurement for each source at the various locations. The orange dots represent the data for the ^{68}Ga source surrounded by water and the blue dots are associated with the ^{22}Na source. The positions to be compared are those aligned along the vertical axis.

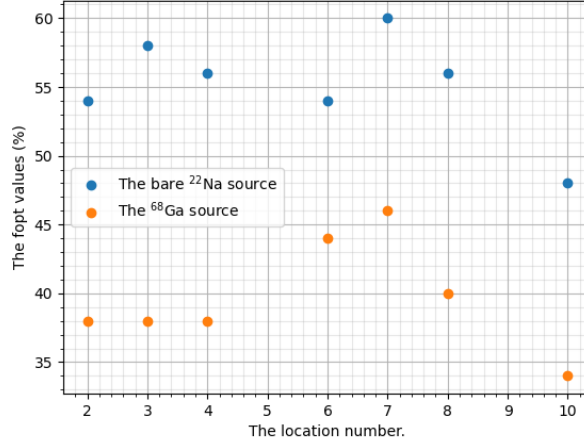


Figure 8: The f_{opt} values at the various locations for the sources.

Figure 7 shows that, as scattering increases, the uncertainty as well as the error measurement also increase. Thus, the precision in the location measured degrades with an increase in scattering. Figure 8 shows that f_{opt} depends on the number of scattered events. As the scattering increases, the f_{opt} values decrease. This is due to the fact that for the ^{68}Ga source, there is an increase in the amount of corrupt events caused by scattering, and the f_{opt} value thus has to be lower in order to discard those events.

6 Sensitivity and Efficiency

6.1 Theory

Measuring the efficiency and sensitivity of the PEPT scanner is very crucial as this will allow us to be able to determine how ‘efficient’ the entire system is at detecting gamma rays of a particular energy. In PEPT efficiency is subdivided into two classes: *intrinsic* and *absolute* efficiency. However, we are only interested in intrinsic efficiency, which is defined as the probability of a photon being detected and recorded once it has entered the detector. This depends only on the individual detector elements and the energy of the photon.

The detector settings can be adjusted so that it only detects events which deposit full energy, as the latter cannot be mistaken for spurious noise and are not sensitive to some perturbing effects such as scattering from surrounding objects. This measurement of the intrinsic efficiency can then be used to evaluate the performance of each individual detector element and check for faults in each of them.

Sensitivity is defined as the probability that a pair of photons emitted from a specified location will be detected in coincidence. Sensitivity changes as a function of position and it is necessary that any possible source location lies directly in line between at least two detectors. We can then evaluate the sensitivity of the system by measuring the number of coincidences detected at different locations. This can be normalised by the number of decays the source undergoes.

For our measurements, we look at the locations seen in figure 6 and table 1.

6.2 Results and Analysis

6.2.1 Sensitivity

After measuring the detector counts, the sensitivity of the detector modules for different locations was found by taking a ratio of the coincidence rate to the activity of the ^{22}Na source with an activity of $12\mu\text{Ci}$ (which is equivalent to 444000Bq).

$$\kappa = \frac{\text{Coincidence rate}}{\text{Activity}}$$

where κ represents the sensitivity. The coincidence rate for each location was measured and the sensitivity was calculated (refer to table 1 in the appendix to see the coincidence rates for each location).

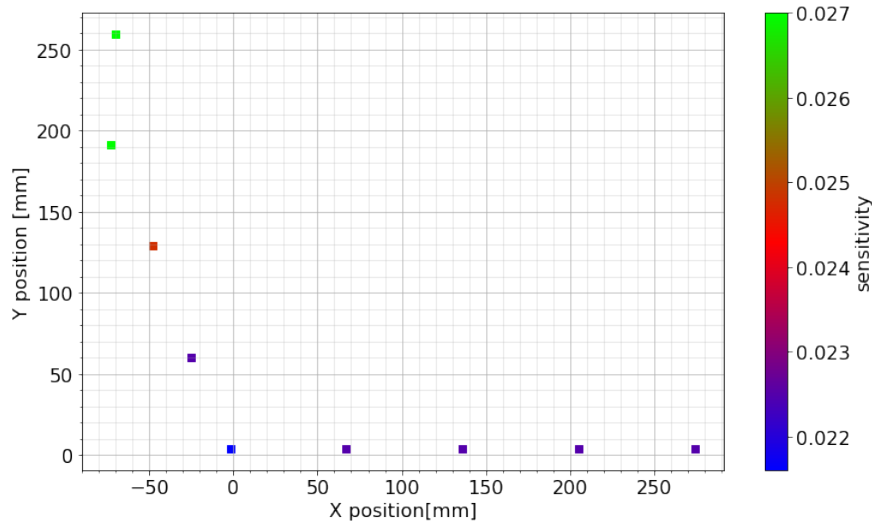


Figure 9: Plot of positions along the xy plane together with their associated sensitivity represented in a colour bar while keeping $z = 0$.

Figure 9 represents a plot of positions x and y with sensitivity changing as the position of the ^{22}Na source is varied. The sensitivity should be at a maximum at the the central

position of the ^{22}Na source but this is not what is observed. Figure 9 shows that the central position gives a sensitivity of $\kappa = 0.0216$, which is the lowest as indicated by the colour map for positions in the xy plane. As the source was moved from the central position the sensitivity increased; this might have been caused by the source being closer to some detector modules, meaning that more gammas were captured as there would be less attenuation due to air and hence an increase in sensitivity. However this explanation does not work entirely, since the distance to other detectors has increased, meaning that more attenuation occurs between those detectors. We also see that even as we move toward the missing detector, the sensitivity still increases, and is in fact at the highest value recorded. This increase in sensitivity makes very little sense, since there would be a smaller solid angle that the detectors take up, meaning that less photons should be incident on the detectors. With our current understanding we can only conclude that something significant must have gone wrong during the measurement process and that repeat measurements should be made.

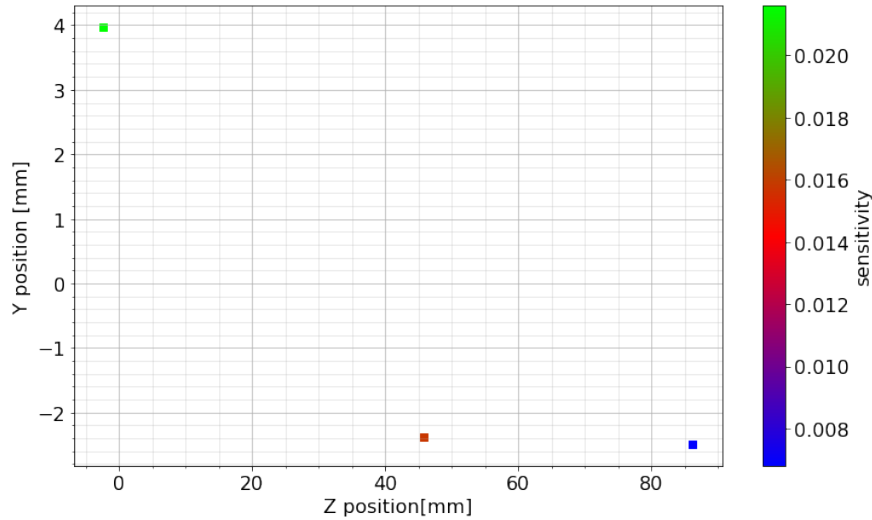


Figure 10: Plot of positions along the yz plane together with their associated sensitivity represented in a colour bar.

In figure 10, there are three positions, with the x and y positions being kept at zero. When the z position is varied, the sensitivity should decrease since the source is being moved away from the detectors and the number of ways in which an LOR can form decrease. The point closest to $z=0$ has a higher sensitivity when compared to the other two points, which is expected, since its location corresponds to where the solid angle subtended by the detectors is at a maximum, and the number of ways in which an LOR can form has been maximised.

6.2.2 Efficiency

After recording all detected photons of a centralised ^{22}Na source with an activity of $12\text{ }\mu\text{Ci}$ over the course of 10 minutes, the program *unroll.exe* was used, which calculates the total number of counts detected in individual crystals. This was then used to plot figure 11. The contrast of the image was increased by setting a limit on the total number of photons that could be detected, producing figure 12.

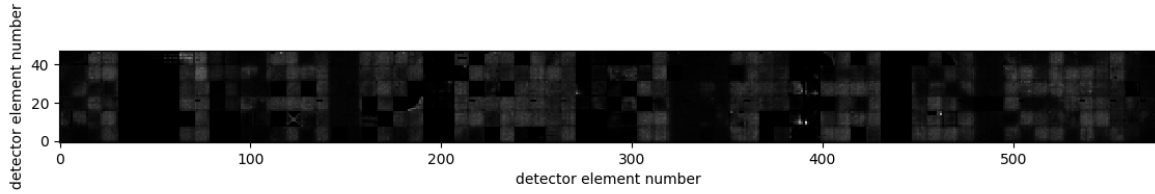


Figure 11: Grey scale (i.e. the brighter, the higher the intensity) image of the number of gamma rays detected for each individual crystal. Each pixel represents a single crystal, each set of 8×8 crystals represents a detector block and each set of 2×6 detector blocks represents a module. The modules are labeled from left to right starting from module 0, up to module 35.

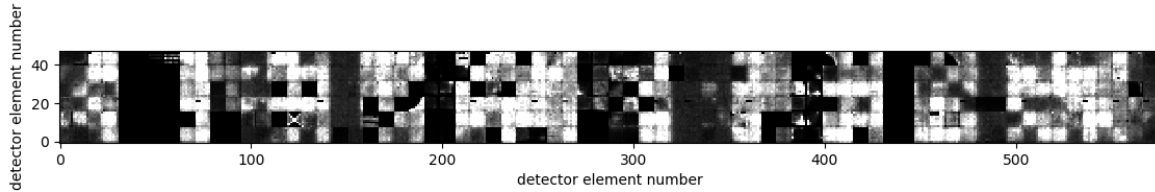


Figure 12: Grey scale image of the number of gamma rays detected for each individual crystal with the contrast decreased (by setting a limit on the total number of gamma rays that can be detected in a single crystal). Each pixel represents a single crystal, each set of 8×8 crystals represents a detector block and each set of 2×6 detector blocks represents a module. The modules are labeled from left to right starting from module 0, up to module 35.

Figure 11 gives a good visual representation of the efficiency of each of the detectors and reveals that a lot of the detectors are not inserting data into the saved files, as shown by the completely black areas. This was expected from modules 2 and 27 as they were not in the gantry at the time of measurement. However, there are also a few dysfunctional detector blocks in most of the modules. This is made a lot clearer by figure 12.

It can be noted that the majority of blocks in module 3 are not working, and some functional blocks have dead crystals within them. Inactive blocks are common throughout the gantry and should be fixed, although it is rather difficult to say what exactly is wrong with each block without more information.

Figure 12 also gives an indication of which blocks are detecting less counts than they should. All the blocks should be able to detect the same amount of gamma rays since the source emits radiation isotropically. However, in figure 12 we can see that this is not the case for our scanner. As observed, some of the detectors detect significantly fewer counts than other functional detectors. For example modules 21 and 20 seem to have a much lower efficiency than the other functional modules. These most likely require non-trivial repairs or replacements to correct.

7 Spatial Resolution

7.1 Theory

Even though PEPT uses a modified PET detector, spatial resolution in PEPT is different from that in PET since we do not aim to image the source, but rather to determine its location (we do not wish to distinguish between two points after image reconstruction) [14]. In this regard, spatial resolution is not as limited by the pixel size in our detector as in the PET case. Therefore, spatial resolution in PEPT is a measure of how well the detector can precisely and accurately determine the instantaneous location of the positron-emitting source via the intersection of multiple LORs between co-incident 511 keV gamma rays. In other words, it is the minimum distance between the location of two detected photons at which their location can be distinguished from one another. If two locations are separated by a distance less than this, they are within each other's uncertainty ranges and are not distinguishable. The two main factors which affect spatial resolution in PEPT are pixel size and positron range [9]. When a photon falls on a pixel, it is unknown exactly where on the pixel the photon was detected, and therefore the larger the pixel, the greater the uncertainty on the location of the source, as depicted in figure 13:

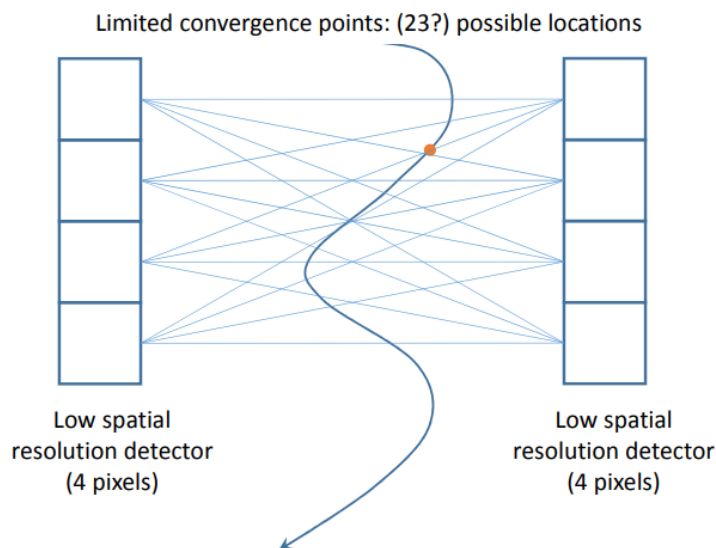


Figure 13: This figure shows an extreme case of very large pixel size and it can be seen that the LORs do not intersect the location of the source nicely; instead, we have the formation of a grid with 23 possible locations for the source. Decreasing the pixel size decreases the size of this grid which more accurately narrows down the possible location of the source.

Positron range refers to the fact that when β^+ emission occurs, the positron emitted travels a certain distance in its medium and loses some momentum, only annihilating once it captures an electron. This means that the point at which the source emits the positron and the point at which annihilation occurs are slightly different. This positron range concept is visualised in figure 14. As we know, the LORs will correspond to the line along which the annihilation occurred and not necessarily where the source is. This contributes to the uncertainty and thus spatial resolution of our detector in determining the location of the source. In order to account for positron range we could have used different radioactive sources that have different positron energies instead of just using ^{22}Na , but unfortunately we did not have access to this.

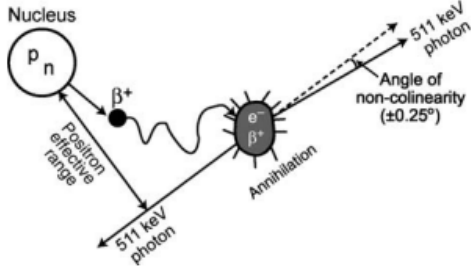


Figure 14: This diagram depicts the concept of positron range where the β^+ particle annihilates a distance from the nucleus. [9]

7.2 Results and Analysis

The same measurements were used for spatial resolution as from previous sections, which is to say that a ^{22}Na source with an activity of $12\ \mu\text{Ci}$ was placed in the locations mentioned in table 1 and figure 6.

After obtaining the data from the detector, *ctrack* was used to extract the data in a text file format. The output file contained information regarding the time, and determined x , y and z positions for each slice of the raw input data. These files gave us multiple determined locations for the source at each of its known positions. A statistical package (scipy stats fit [8]), which uses maximum likelihood estimators in Python, was then used to fit a Gaussian distribution to the data and extract the Gaussian parameters for the x , y and z axes for each of the positions used. One of these parameters was the standard deviation (σ), which was then used to calculate the Full width at half-maximum (FWHM), which will be quoted as our spatial resolution: $FWHM = 2.355\ \sigma$

Figures 15, 16 and 17 show the Gaussian fitting for the source placed at the origin:

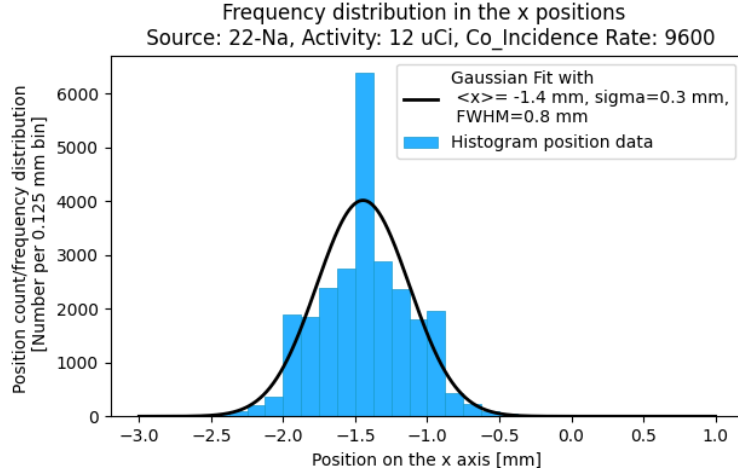


Figure 15: A histogram showing the number of locations determined by *ctrack* vs the positions along the x -axis, with a Gaussian distribution fitted over it for the source located at location 1: origin (0,0,0). The standard deviation determined is 0.3 mm and the FWHM (and thus spatial resolution) is 0.8 mm.

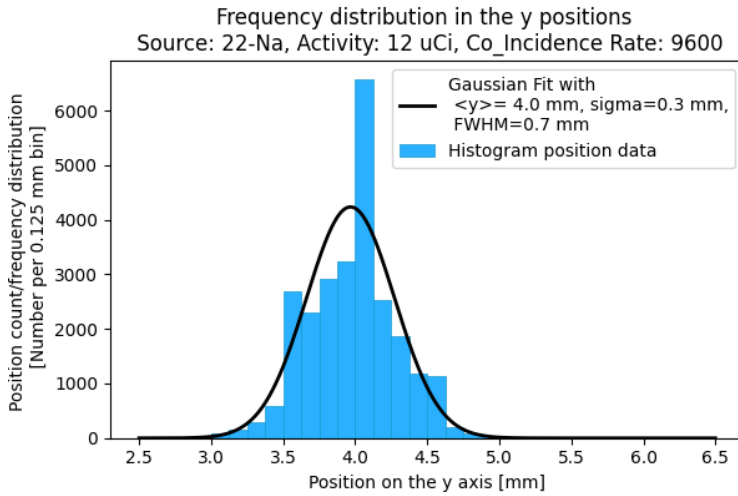


Figure 16: A histogram showing the number of locations determined by *ctrack* the positions along the y -axis, with a Gaussian distribution fitted over it for the source located at location 1: origin (0,0,0). The standard deviation determined is 0.3 mm and the FWHM (and thus spatial resolution) is 0.77 mm.

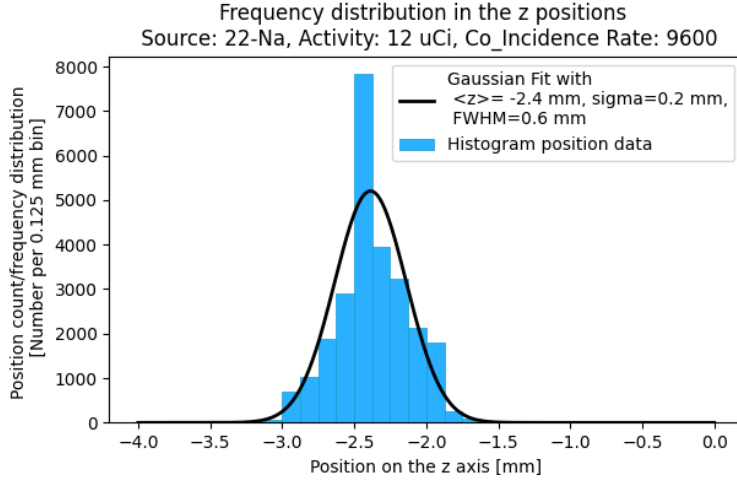


Figure 17: A histogram showing the number of locations vs the positions along the z -axis determined by *ctrack*, with a Gaussian distribution fitted over it for the source located at location 1: origin (0,0,0). The standard deviation determined is 0.2 mm and the FWHM (and thus spatial resolution) is 0.6 mm.

$\langle x \rangle$	FWHM x	$\langle y \rangle$	FWHM y	$\langle z \rangle$	FWHM z	Combined FWHM	N_{Events}
-1.4 mm	0.8 mm	4.0 mm	0.7 mm	-2.4 mm	0.6 mm	1.2 mm	25 921
135.9 mm	0.9 mm	3.5 mm	0.8 mm	-5.6 mm	0.6 mm	1.3 mm	13 688
274.3 mm	1.4 mm	3.4 mm	0.9 mm	-7.4 mm	0.6 mm	1.8 mm	12 781

Table 2a

$\langle x \rangle$	FWHM x	$\langle y \rangle$	FWHM y	$\langle z \rangle$	FWHM z	Combined FWHM	N_{Events}
-1.4 mm	0.8 mm	4.0 mm	0.7 mm	-2.4 mm	0.6 mm	1.2 mm	25 921
-0.9 mm	0.8 mm	-2.4 mm	0.8 mm	45.9 mm	0.6 mm	1.3 mm	9 590
-1.4 mm	1.2 mm	-2.8 mm	1.1 mm	94.6 mm	0.9 mm	1.9 mm	4 524

Table 2b

Figure 18: Table 2a shows the average x , y and z values of the determined positions of the source for locations 1, 2 and 3 (moving along the x -axis while z and y remain at 0) respectively, as well as the FWHM (spatial resolution) at the x , y , z positions. Table 2b shows the average x , y and z values of the determined positions of the source for locations 1, 4 and 5 (moving along the z -axis while x and y remain at 0) respectively, as well as the FWHM at the x , y and z positions.

As we can see from the figure 18 above, spatial resolution increases along the x and z -axis (and by symmetry the y -axis) as we move outward from the origin, as expected.

8 Image Quality

8.1 Theory

One way to evaluate the ability of the system to reliably record data and construct an image is to record a known source setup and observe the precision associated with the measured location of the source. This comparison can be done before the image reconstruction as a means of evaluating the spatial resolution [7](#), or can be done after image reconstruction as a catch-all means of finding all irregularities in the image.

The sinogram matrix will display information on all the recorded coincidence events for a given plane in the z-axis. For each detected coincidence a sinogram is constructed by measuring the distance of the LOR from the centre of the FOV and determining the angle from a set polar origin and recording these as the amplitude and phase on a sine function respectively - see A and B in figure [19](#). When many coincidences are recorded, this results in many fully formed sine functions (C in figure [19](#)), each containing the information about the location of a single coincidence source. If we have a distribution of source this process is done for each radiating point up to the resolution limits of our detector - and the superposition of all of this information is our full sinogram map. To reconstruct the image from the sinograms, we use a Radon integral transform [\[4\]](#) - resulting in an image like the one in D of figure [19](#).

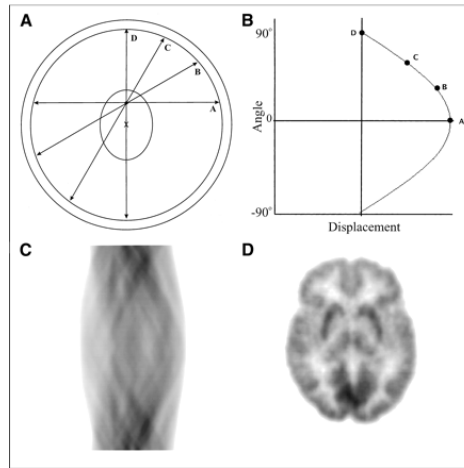


Figure 19: Diagrams of the PET imaging process through sinograms [\[11\]](#).

Any coincidence failure or detector fault will be clearly visible in the sinogram data as dark stripes - areas of much lower count rates. Other abnormalities visible in the sinogram, such as bright spots, can also be due to detector setup faults causing abnormally high count rates from a certain position.

From the sinograms we can reconstruct the image of the source within the FOV.

Comparison between the reconstructed image and the actual source setup will further tell us about faults and abnormalities within our system. Furthermore, we can evaluate some level of uncertainty in our reconstructed image of the source.

8.2 Method and Analysis

The measurements of the coincidences produced by a stationary ^{22}Na of activity $12\ \mu\text{Ci}$ source located at the origin were analysed.

The 2D sinogram produced by a centralised $12\ \mu\text{Ci}$ ^{22}Na source recorded over the course of 10 minutes is shown in figure 20. The contrast of the image was then decreased by setting a cap on the total number of coincidences that can be assigned to any particular pixel, allowing us to produce figure 21. It can be noted that these sinograms were produced by summing all the 2D sinograms along the axial plane of which there were 95.

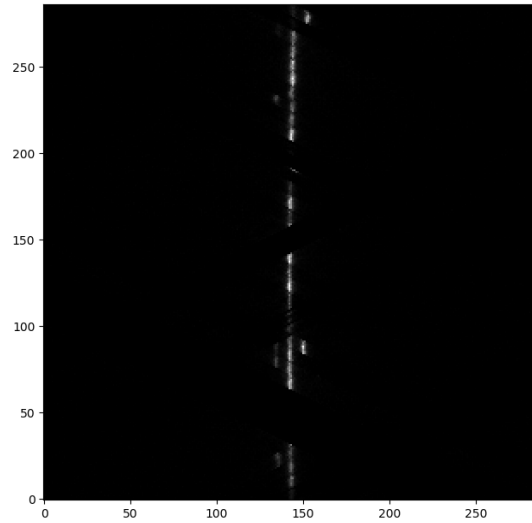


Figure 20: A 288×288 pixel sinogram of a centralised $12\ \mu\text{Ci}$ ^{22}Na source recorded over 10 minutes.

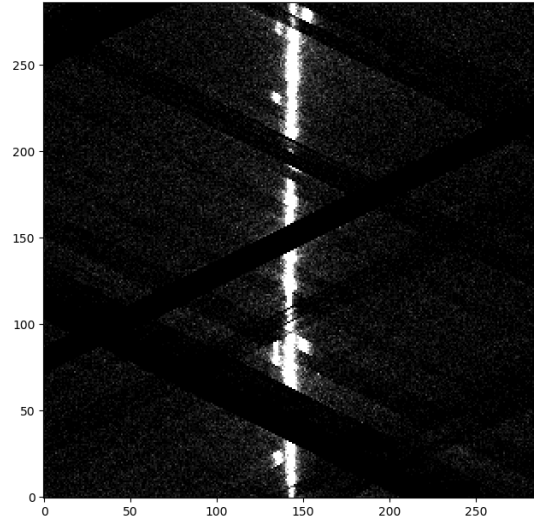


Figure 21: A 288×288 pixel sinogram of a centralised $12 \mu\text{Ci } ^{22}\text{Na}$ source recorded over 10 minutes with the contrast decreased by setting a limit on the total number of LORs that can be associated with each pixel.

Figures 20 and 21 reveal a large number of issues with the system. The black diagonal stripes are indicative of missing detectors, of which there are a few and this, along with most issues, has already been discussed in section 6. A problem that we can identify almost exclusively in these sinograms however, is some of the artefacts produced near the central white line. These are not supposed to be here but are rather supposed to be aligned with the central line. A possible cause of these modules producing artefacts to a sinogram in such a manner is if the blocks/analogue boards are connected incorrectly, i.e. if the module is ‘upside-down’, or if the blocks are connected to the wrong photomultiplier tube. These issues should be fixed by connecting the blocks correctly.

Setting aside these issues for now, but keeping them in mind, we can then use these sinograms to reconstruct an image using a radon transform [4] and other filtering methods [3]. Once that is done, we can construct the point spread function (PSF), which gives a measure of the sum of the intensity along a particular axis, along the horizontal plane and vertical plane, which can all be seen in figure 22.

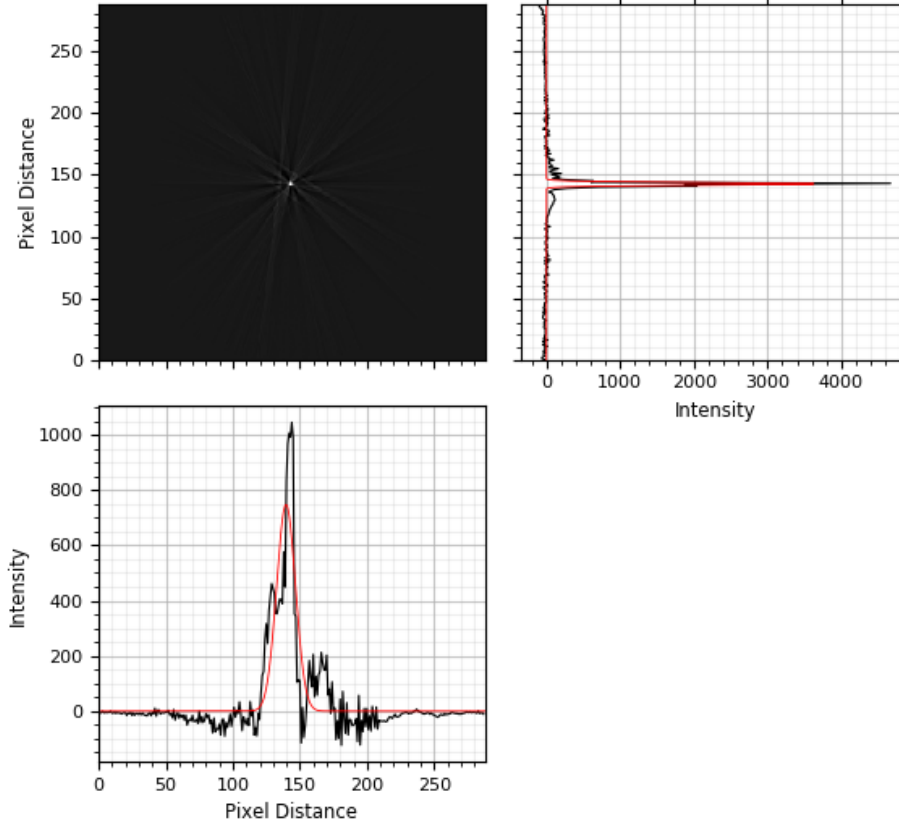


Figure 22: 288x288 pixel reconstructed image of the sinogram in figure 20 with horizontal PSF located beneath the reconstructed image and vertical PSF located to the right of the reconstructed image. The dark lines in the PSFs represent the measured sum of intensity along the corresponding row/column for the vertical/horizontal PSFs and the red lines represent the fitted Gaussian.

Now analysing the reconstructed image and its PSFs from figure 22, we first note that the vertical PSF has nothing noticeably wrong with it, which is to say that there is a clear Gaussian distribution that forms, with a central position $\mu = 142.61$ pixels and with standard deviation $\sigma = 1.09$ pixels. Or, in other words, the position of the source along the vertical axis is $y = 142.61 \pm 1.09$ pixels at a 68% confidence interval. This implies that the fitting is of a good quality and since the width of this Gaussian is so small, the position of this particle is well known with high precision. However, the horizontal PSF has quite a few problems in comparison with the Gaussian being a lot less defined and the position of the source along the horizontal axis being calculated to be $x = 139.73 \pm 7.03$ pixels at a 68% confidence interval. The horizontal standard deviation is 7 times larger than the vertical standard deviation which is problematic. We also note that the measured PSF has a lot of areas where the intensity unexpectedly

increases by a significant amount. This and the large uncertainty on the position are most likely due to all the problems discussed previously in this section and in section 6, where detectors were connected improperly and some modules and blocks were not functioning well. The biggest contributor is most likely the missing modules since modules 2 and 3 (which is very damaged as seen in figure 12) are located near the top of the HR++ and module 27 near the bottom of the detector. This leads us to conclude that if the source is located in a central position, these missing modules would play almost no role in calculating the vertical position which explains why the vertical PSF is still good in comparison.

9 Accuracy and Precision

9.1 Theory

The accuracy of the scanner measurement refers to how close the measured position of the tracer particle is to its known position. Being able to quantify the accuracy of the scanner is important as it will indicate how close measurements of position taken by the scanner are to the known position values. This is fundamental in characterizing the scanner and validating it as a reliable measuring instrument. It would also be useful to know how the accuracy of the scanner varies as a function of position, which could help with optimising measurements. The percentage accuracy A is related to the difference in the measured and known position via

$$A = \left(1 - \frac{|x - p|}{p}\right) \times 100\% \quad (5)$$

where x is the measured position and p is the known position. For measurements, provided that the source remains in the scanners field of view, its accuracy should be independent of the position of the source in the scanner. The precision however, will be dependent on position. Precision refers to how close two or more position measurements are to one another (defined as the quality of being exact). Measurements will be most precise in the centre, with the precision decreasing as the source moves to the edges.

9.2 Method

Investigations into the accuracy of the scanner involved a series of measurements of a point source at different known positions. Comparing the measurements to the known positions gave an indication of the accuracy of the measurements. For PEPT, calculating the standard deviation σ of the measurements obtained made it possible to qualitatively describe the precision of the measurements. For PET, the distortion in the image of the particle was a qualitative measure of the precision of the image produced.

9.3 Analysis

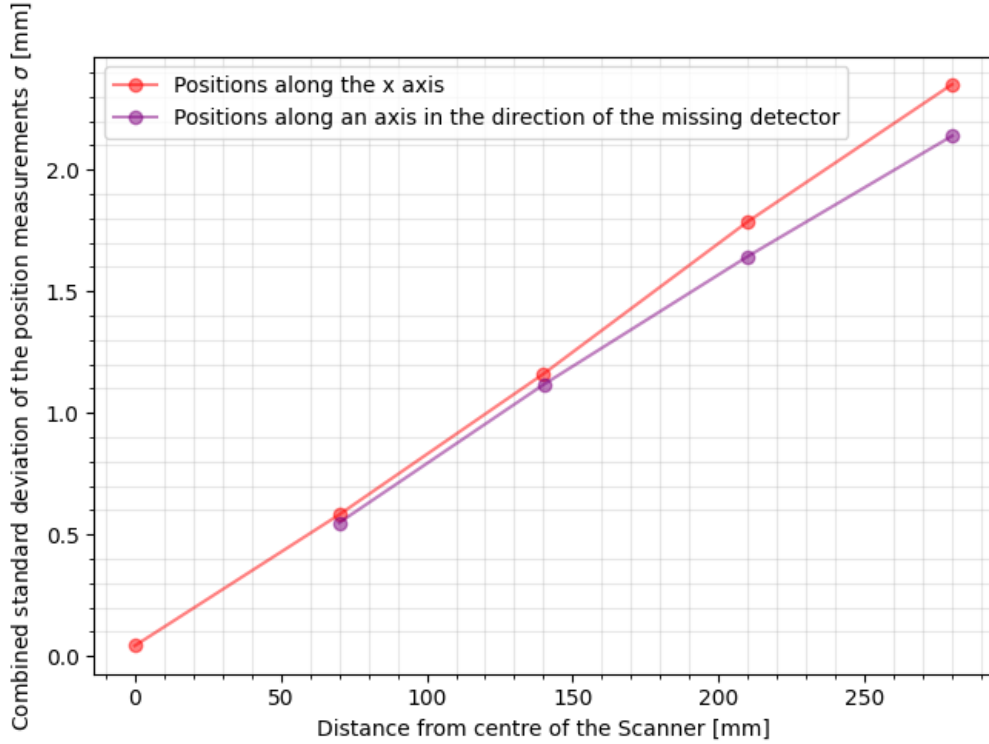


Figure 23: Graph displaying how the combined standard deviation σ of the measured position changes as a function of the known position. The red plot shows how σ changes as only the position along the x -axis is varied. The purple plot shows how σ changes as only position along an axis in the direction of the missing detector is varied.

For PEPT, figure 23 displays the standard deviation σ of the position of the particle as a function of the known position along the x -axis (red plot) and in the direction of the missing detector (purple plot). The standard deviation of the data represents how much the data deviates away from the mean value, which is another way of qualitatively describing the precision of a measurement. From fig 23, when moving along the x -axis only, it can be seen that σ increases, indicating that the precision of the measurements decreases. The same behaviour can be seen when changing the position of the particle along the direction of the missing detector. The behaviour of the standard deviation when moving along the z -axis is not shown due to too few data points, however the same trend was observed. It is safe to then conclude that the precision of the measurements decreases as the particle is moved further away from the centre of the scanner. Not only does the standard deviation increase, but it increases in a linear fashion. It does so faster for measurements taken at positions along the x -axis compared to measurements taken along an axis in the direction of the missing detec-

tor. This could be explained by there being fewer changing levels of statistics in the direction of the missing detector compared to that in the direction of the x -axis.

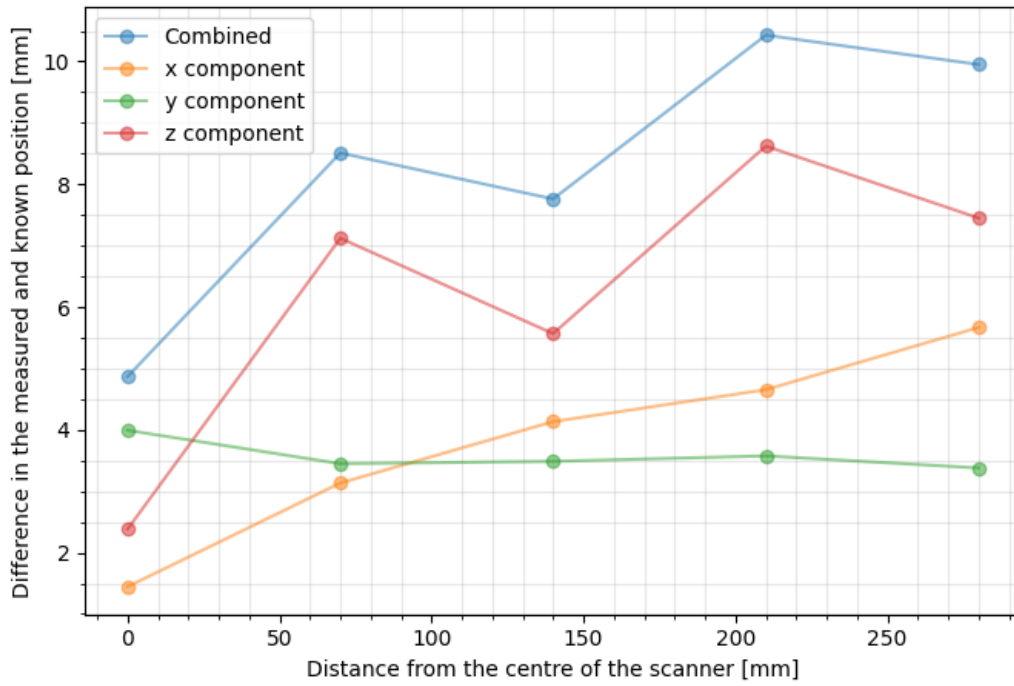


Figure 24: Graph displaying how the difference between the measured and known position changes as a function of the known position along the x -axis. The graph contains plots displaying this difference in each dimension (x , y , z) and the combined difference consisting of all three dimensions.

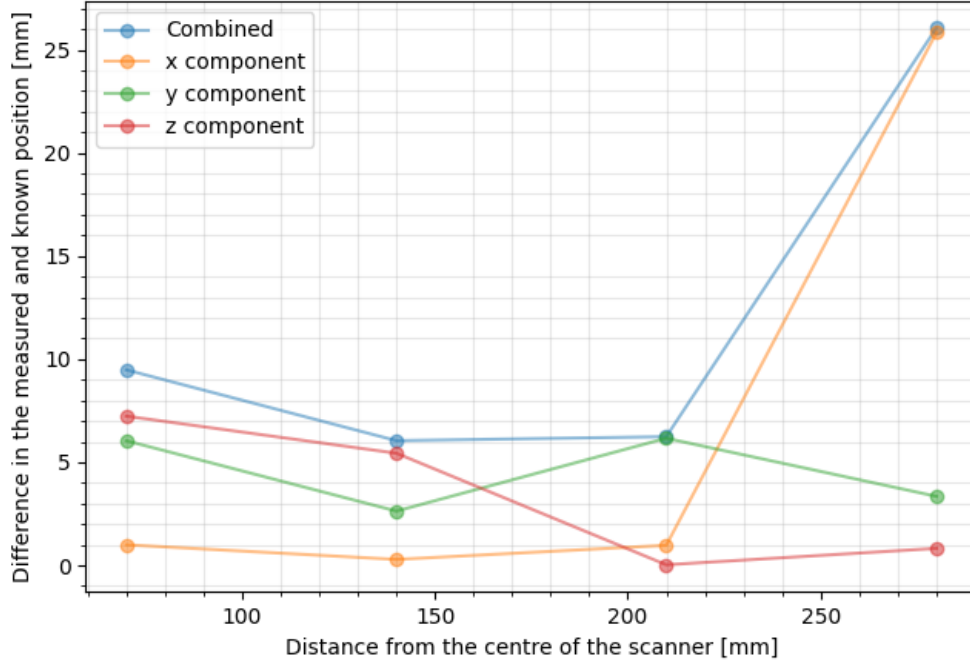


Figure 25: Graph displaying how the difference between the measured and known position changes as a function of the known position along an axis in the direction of the missing detector. The graph contains plots displaying this difference in each dimension (x , y , z) and the combined difference consisting of all three dimensions.

Theoretically, the accuracy should be independent of position in the detector, however, from figures 24 and 25, it is clear that this is not the case. In figure 24, the differences between the measured and known position of the particle when the position along the x -axis is varied is shown. It can be seen that the difference in position tends to increase as the position of the measured particle is further away from the centre of the scanner. The difference in the x -direction (orange plot) increases as the position is moved further away from the origin. Since the difference in known and the measured position is inversely related to the accuracy of the measurement, it is evident that the accuracy of the measurements decreases as the particle is moved further away from origin, which contradicts the theoretical prediction. The difference in the y -direction (green plot) remains relatively constant. The difference in the z -direction (red plot) however, dominates the change in the difference of position, and is the main contributor to the sporadic increasing form of the combined difference in position (blue plot).

In reference to fig 25, not much can be said about the accuracy of the measurements when changing the position in the direction of the missing detector. This is due to the

error in measuring the known value at the furthest position away from the origin in the scanner, due to the reference lasers not being visible at high y -positions. However, when ignoring that measurement, it can be seen that once again the difference in the z -direction is the greatest contributor to the overall accuracy behaviour, and is mostly responsible for the change in accuracy as a function position.

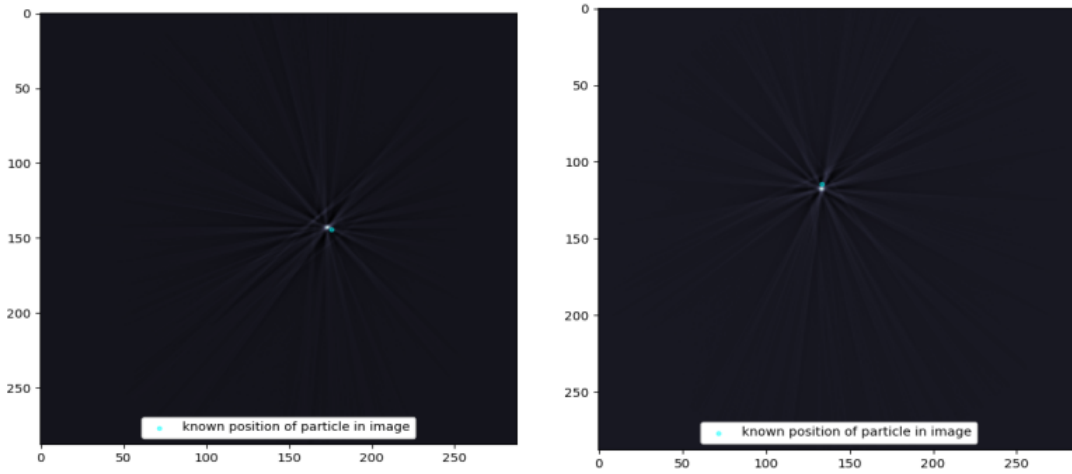


Figure 26: PET Image of the particle with a cyan dot representing the known position of the particle in the scanner. a) (left) Image when the particle is placed in the scanner at position (70, 0, 0) mm. b) (right) Image when the particle is placed in the scanner at position (-23.9, 65.8, 0) mm.

For PET, the accuracy of the stationary sources can be evaluated by comparing the position of the image of the particle to where the image of the particle should be. The expected position of the image of the particle can be determined by multiplying the known position by a scaling factor s ,

$$s = \frac{n}{2R} = \frac{288 \text{ px}}{2(320 \text{ mm})} \quad (6)$$

where n is the number of pixels per side and R is the radial field of view of the scanner. This value is then shifted so that the axis aligns with the image's axis. Figures 26 and 27 show images of the particle at positions 70 mm from the centre of the scanner and 280 mm from the centre of the scanner respectively, along the x -axis and along an axis in the direction of missing detector 2. The cyan dot represents the known position of the particle. These figures show that the image of the particle becomes more distorted, thus less precise, as the position gets further from the centre. The point spread function for some of these images are shown and discussed in section 8. A point of note is that there is not a significant difference in precision when comparing the images of the particle a distance from the centre in the direction of the missing

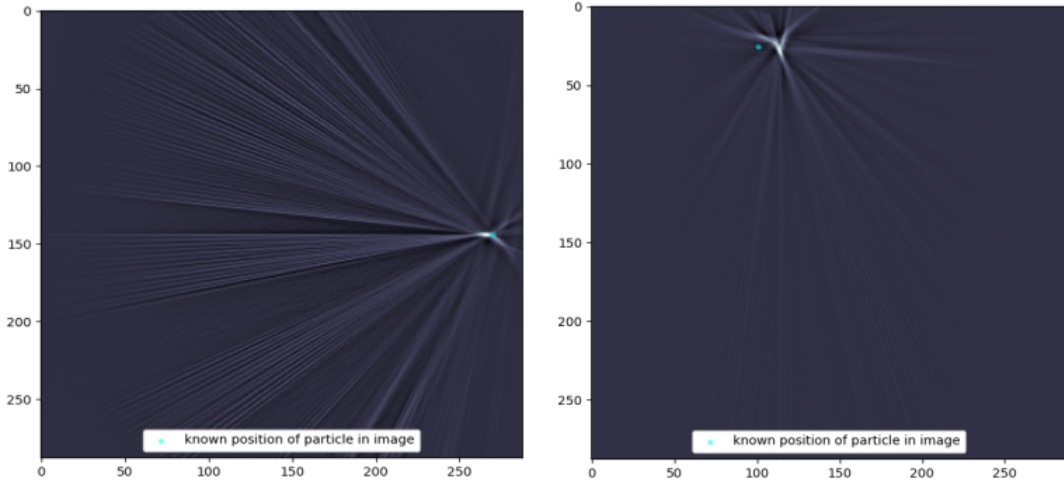


Figure 27: PET Image of the particle with a cyan dot representing the known position of the particle in the scanner. a) (left) Image when the particle is placed in the scanner at position (280, 0, 0) mm. b) (right) Image when the particle is placed in the scanner at position (-95.8, 263.1, 0) mm.

detector to those the same distance from the centre but along the x -axis. This implies that the visual precision is not significantly affected by whether the measurements are taken near the missing detector.

The distance between the known position of the particle and the image of the particle, which is an indication of the accuracy, remains fairly constant, with a slight increase as the distance from the centre increases. The largest deviations occur at the furthest positions, specifically in the direction of the missing detector. This deviation can be attributed to the uncertainty in measuring the known position of the particle, which increases at positions further from the centre, since the lasers used as a reference for the measurements were not visible. The magnitude of the accuracy is also affected by the scaling factor. The accuracy and precision of the radial field of view were unknown. A better method for determining this scaling factor would have produced more reliable results for accuracy in the PET images, for example placing the particle at a specific position and then moving it a distance which can be reliably measured and comparing this to how much the image of the particle is shifted to determine the pixel-to-mm scaling factor and shift.

10 Deadtime

10.1 Theory

Deadtime refers to the period of time after an event is detected, during which a detector is unable to detect a new event and is characterised by the "deadtime parameter". This particularly affects the detector system at high activities, causing the measured count rate to reduce from the true count rate. There are two different kinds of deadtime [21], namely paralyisable and non-paralyisable deadtime. For the purposes of this report, only the non-paralyisable deadtime parameter will be determined, which assumes that a fixed time τ_{np} follows each true event [21]. Events which occur during this time period will have no effect on the detector response.

10.2 Method

In order to measure the deadtime of the HR++ scanner, the measured singles count rate and the activity of a high activity source would need to be measured. In this experiment, a liquid solution of ^{68}Ga , which has a half-life of 1 hour, was used as the decay source. Prompt and delayed measurements for each run were required in order to obtain the true singles count rate [13]. The goal was to obtain these measurements for both an on-centre and off-centre source, in order to compare deadtime effects for different experimental setups. The data which we hoped to obtain would consist of 34 measured count rates for each run, one for each of the working modules. The most efficient module would then be chosen out of the 34, and the count rate of the same module would be used in the analysis of the deadtime for the centred and off-centre sources. This choice of module be achieved by plotting a graph of the log singles rate as a function of time for each of the modules, and determining which of the modules has the most consistent singles rate. This process is shown in figure 28 for data taken several years ago.

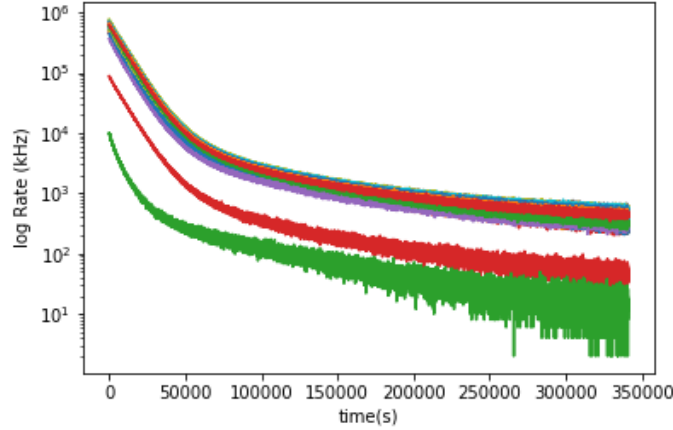


Figure 28: The figure above shows the log singles rate as a function of time for the 34 modules, using data that was taken some time ago.

Once the most consistent module was obtained, the measured count rate as a function of activity would be plotted. Fitting a curve to this count rate data would allow one to model the decay of the source, and from the fitted curve, the deadtime parameter could be determined [13],[2]. The model is of the form:

$$R_p = \frac{S}{S\tau_{DT}}$$

Where R_p is the recorded singles rate, S is the singles rate if deadtime were not present and τ_{DT} is the deadtime parameter [13]. The true singles rate would also be plotted, but would appear as a straight line due to the fact that it does not take deadtime into account.

10.3 Analysis

Unfortunately, due to load-shedding, the data needed to perform the analysis detailed in section 10.2 could not be obtained, and data was only obtained for a central source. Measurements were taken in 10 second intervals in steps of 100 μC until a total of 1000 μC had been added to the vial. 200 μC was added per step. The measurements obtained were of the prompt and delayed values, with no singles data being obtained. Using the prompt and delayed values, the true count rate was obtained:

$$C_{True} = C_{Prompt} - C_{Delayed}$$

Where C_{True} is the true count rate, C_{Prompt} is the rate of Prompt coincidences and $C_{Delayed}$ is the rate of Delayed coincidences. The count rate was plotted as a function of activity, and is shown in figure 29. What one would expect to observe is that, for high activity, the relationship between the count rate and activity should deviate from

a linear relationship, due to the effects of deadtime. The expectation is thus that the data obtained will be linear at lower activity, before becoming non-linear for higher activity.

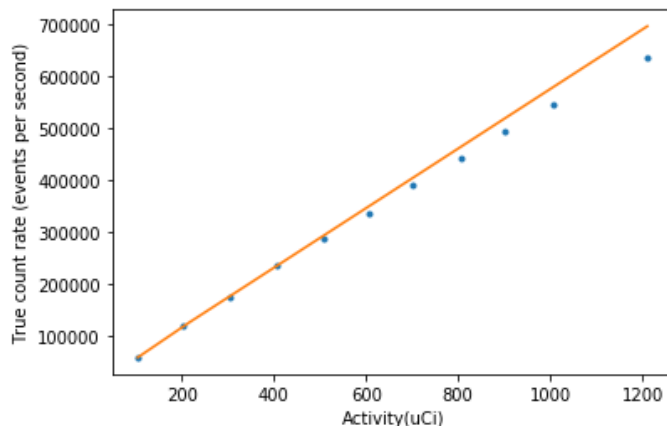


Figure 29: Figure 29 above shows the True count rate as a function of activity for the liquid ^{68}Ga . A linear ‘expected’ response was plotted - this is the orange line - which was fitted to the data at low activities, and extrapolated to higher activities. From this, we see that the data deviates slightly from this line at higher activities.

The slight deviation of the data from the straight line in figure 29 is due to deadtime. Unfortunately, the deviation is so small that it is not adequate to determine a deadtime parameter. A greater activity would need to be reached in order for the effects of deadtime to be more visible, and due to load-shedding, this was simply not possible. In future experiments, we would hopefully be able to take measurements for a longer period of time so that a sufficiently high activity could be reached, which would allow us to observe the effects of deadtime on our data.

11 Conclusions

The optimal fractional value for a centralised ^{22}Na source was obtained and it was found that $f_{opt} = 50$ for a stationary particle. Figure 4 showed that there is an inverse relationship between the 3D standard uncertainty and the events per slice.

It was concluded in the Randoms analysis that sources of less than or equal to 1200 μCi were reasonable to image or collect PEPT related data from. The point at which the randoms may overwhelm the prompts was not reached within the scope of this experiment.

For scatter fraction, it was found from figure 7 that as scattering increases, the uncertainty and the error measurement increase as well, which degraded the precision in location. Additionally, it was shown from figure 8 that the f_{opt} depends on the number of scattered events. An increase in scatter saw a decrease in the f_{opt} values, which can be attributed to the fact that for the ^{68}Ga source there is an increase in the amount of corrupt events because of the scatter and so f_{opt} has to be lower in order to discard those events.

The graph in figure 9 shows the sensitivity of the source at different positions. Ideally, the sensitivity should be at a maximum at the central position. However, figure 9 shows that the sensitivity is at a minimum at the central position, possibly because the source moved closer to other detector modules when moved from the central position. When the z position is varied, figure 10 shows that the sensitivity decreases since the source is being moved away from the detector modules. Following this, a thorough analysis of the efficiency was given. Figure 12 in particular showed that certain detector blocks within the modules were not working, which gave a clear indication of which blocks were detecting less counts than they should.

The spatial resolution was then determined at the origin of the detector in the x , y and z coordinates, and was found to be $< 0.8, 0.7, 0.6 >$ mm. It was evident that the further away from the origin, the higher the spatial resolution was, as expected.

It was shown in the Image quality analysis that the horizontal PSF was problematic and was not as well defined as the vertical PSF for a centralised source, as shown in figure 22. It was concluded that this was due to the missing and damaged modules, which should be fixed. It was also seen that quite a few of the detector blocks were improperly connected as seen in figures 21 and 20 and that this issue should also be addressed in order to improve precision.

For PEPT, the data indicated that there was a dependence of the accuracy of the scanner measurement on the position of the particle. Furthermore, as the position of the particle is moved further away from the origin, the accuracy of the measurement of its position decreases, contradicting the theoretical expectation. However, for PET, the accuracy remains relatively independent of position. For both PEPT and PET,

evidence shows that the precision of a measurement of position decreases at positions further away from the centre of the scanner, supporting the expectation of the the precision being dependent on position. Collection of more data at a larger variety of positions would aid in obtaining more definite results and overall improve the quality of the investigation.

With regard to deadtime, due to load-shedding and other factors, the data that was acquired from iThemba labs was not sufficient to determine the deadtime parameter. Figure 29 displays a graph of the True count rate as a function of activity. The data showed a slight deviation from the linear expected response at higher activities, but these were not high enough to obtain this parameter.

References

- [1] Buffler. A; Govender. Indresan; Cilliers. J; Parker. D; Franzidis. J-P; Mainza. Aubrey. “PEPT Cape Town: A new positron emission particle tracking facility at iThemba LABS.” In: *International Topical Meeting on Nuclear Research Applications and Utilization of Accelerators*. (2009).
- [2] T; Buffler A.; Cole. K.; Leadbeater and M. van Heerden. “Positron emission particle tracking: A powerful technique for flow studies.” In: *International Journal of Modern Physics: Conference Series* 48 (2018).
- [3] Ian Burke. *Sinogram-to-Image*. URL: <https://github.com/IanB14/Sinogram-to-Image>.
- [4] Ralph Brinks; Thorsten Buzug. *Image reconstruction in positron emission tomography (PET): the 90th anniversary of Radon’s solution*. URL: <http://citeseerx.ist.psu.edu/viewdoc/download?doi=10.1.1.556.4321&rep=rep1&type=pdf>.
- [5] et al. Chen S. Hu P. “Performance characteristics of the digital uMI550 PET/CT system according to the NEMA NU2-2018 standard.” In: *EJNMMI Phys* 43.7 (2020), pp. 10–18. DOI: [10.1088/0957-0233/22/10/104017](https://doi.org/10.1088/0957-0233/22/10/104017). URL: <https://doi.org/10.1186/s40658-020-00315-w>.
- [6] et. al Chetty. T. Dikole. R. *Grappling with Granular Gallimaufries*. 2019. URL: <https://vula.uct.ac.za/access/content/group/275677d7-258c-4507-b368-7cb674c91ca0/Laboratory/Lab%5C%207%5C%20-%5C%20groups/PEPT/PreviousY3/PEPT2019report.pdf>.
- [7] et al. Demir Mustafa Sönmezoglu Kerim. “Evaluation of pet scanner performance in pet/mr and pet/ct systems: Nema tests.” In: *Molecular Imaging and Radionuclide Therapy*. 22.10 (2018), pp. 10–18. DOI: [10.1088/0957-0233/22/10/104017](https://doi.org/10.1088/0957-0233/22/10/104017).
- [8] *Docs.scipy.org*. 2021. URL: [https://docs.scipy.org/doc/scipy/reference/generated/scipy.stats.rv\\$%5C_\\$continuous.fit.html..](https://docs.scipy.org/doc/scipy/reference/generated/scipy.stats.rv$%5C_$continuous.fit.html..)
- [9] Saha. G. “Basics of PET imaging.” In: *New York: Springer* (2010).
- [10] *Instrumentation—PEPT Cape Town*. 2021. URL: <http://www.peptcapetown.uct.ac.za/pept-cape-town/instrumentation>.
- [11] Leadbeater. T. W.; Parker. D. J.; Gargiuli J. “Data Acquisition in PET Imaging”. In: *Journal of Nuclear Medicine Technology* (2002), pp. 39–49. URL: <https://tech.snmjournals.org/content/30/2/39#F5>.
- [12] T.W. Leadbeater. *UCT HR++ positron camera documentation*. 2021.

- [13] Gargiuli J Leadbeater. T. W. Parker. D. J. “Characterization of the latest Birmingham modular positron camera”. In: *Measurement Science and Technology* 22.10 (2011), p. 104017. DOI: [10.1088/0957-0233/22/10/104017](https://doi.org/10.1088/0957-0233/22/10/104017). URL: <https://iopscience.iop.org/article/10.1088/0957-0233/22/10/104017> (visited on 10/31/2021).
- [14] H. Olaya Davila¹; C. Morel; H. F. Castro³; S. A. Martinez Ovalle. *Determination of Spatial Resolution of Positron Emission Tomograph of Clear PET-XPAD3/CT System*. 2016.
- [15] *Positron Emission Particle Tracking (PEPT) overview*. URL: <https://www.birmingham.ac.uk/research/activity/physics/particle-nuclear/positron-imaging-centre/positron-emission-particle-tracking-pept/pept-overview.aspx>.
- [16] *Scatter Fraction- Emission Tomography*. 2021. URL: <https://www.europeanmedical.info/emission-tomography/scatter-fraction.html>.
- [17] C.W. Stearns et al. “Random coincidence estimation from single event rates on the Discovery ST PET/CT scanner”. In: *2003 IEEE Nuclear Science Symposium. Conference Record (IEEE Cat. No.03CH37515)*. Vol. 5. ISSN: 1082-3654. 2003, 3067–3069 Vol.5. DOI: [10.1109/NSSMIC.2003.1352545](https://doi.org/10.1109/NSSMIC.2003.1352545).
- [18] “Testing PEPT Algorithm on a Medical PET Scanner.” In: *Journal of Applied Sciences* (2008), pp. 1738–1743.
- [19] Joseph Gargiuli Thomas W. Leadbeater David J. Parker. *Positron imaging systems for studying particulate, granular and multiphase flows*. URL: <https://www.sciencedirect.com/science/article/abs/pii/S1674200111002148>. (accessed:22.10.2021).
- [20] Joseph Gargiuli Thomas W. Leadbeater David J. Parker. *Positron imaging systems for studying particulate, granular and multiphase flows*. URL: <https://www.sciencedirect.com/science/article/abs/pii/S1674200111002148>. (accessed:23.10.2021).
- [21] Leadbeater. T. W. “A generic singles and coincidence count rate model, including deadtime factors.” In: (2020).
- [22] Leadbeater. T. W. “The development of positron imaging systems for applications in industrial process tomography.” In: (2009).

Appendix

Location Number	Source Co-ordinates (x,y,z) (cm)	Coincidence rate (s^{-1})	Sensitivity κ
1	(0,0,0)	9600	0.0216
2	(7,0,0)	10000	0.0225
3	(14,0,0)	10000	0.0225
4	(21,0,0)	10000	0.0225
5	(28,0,0)	10000	0.0225
6	(-2.39,6.58,0)	10000	0.0225
7	(-4.79,13.16,0)	11000	0.0248
8	(-7.18,19.73,0)	12000	0.0270
9	(-9.58,26.31,0)	12000	0.0270
10	(0,0,5)	7000	0.0158
11	(0,0,10)	3000	0.00675

Table 1: The location, coincidence rate and sensitivity of the ^{22}Na source with an activity of $12\ \mu\text{Ci}$ at different positions of the within the HR++ each of which were recorded over the course of 5 minutes.